1 *In-situ* Lu – Hf geochronology of calcite

2 Alexander Simpson[1,2], Stijn Glorie[1,2], Martin Hand[1,2], Carl Spandler[1], Sarah Gilbert[3], Brad Cave[1]

3 [1]Department of Earth Sciences, School of Physical Sciences, The University of Adelaide, Adelaide SA-5005, Australia
4 [2]Mineral Exploration Cooperative Research Centre (Minex CRC), The University of Adelaide, Adelaide SA-5005, Australia
5 [3]Adelaide Microscopy, The University of Adelaide, Adelaide SA-5005, Australia

6 *Correspondence to*: Alexander Simpson (alexander.simpson@adelaide.edu.au)

7 **Abstract.** The ability to constrain the age of calcite formation is of great utility to the Earth Science community, due to the

8 ubiquity of calcite across a wide spectrum of geological systems. Here, we present the first in-situ laser ablation inductively

9 coupled tandem mass spectrometry (LA-ICP-MS/MS) Lu–Hf ages for calcite, demonstrating geologically meaningful ages for

10 IOCG and skarn mineralisation, carbonatite intrusion and low grade metamorphism. The analysed samples range in age

11 between ca. 0.9 Ga and ca. 2 Ga with uncertainties between 1.4% and 0.5% obtained from calcite with Lu concentrations as

12 low as ca. 0.5 ppm. The Lu–Hf system in calcite appears to be able to preserve primary precipitation ages over a significant

13 amount of geological time, although further research is required to constrain the closure temperature. The in-situ approach

14 allows calcite to be rapidly dated while maintaining its petrogenetic context with mineralization and other associated mineral

15 processes. Therefore, LA-ICP-MS/MS Lu–Hf dating of calcite can be used to resolve the timing of complex mineral

16 paragenetic sequences that are a feature of many ancient rock systems.

1 Introduction

18 Suspendisse Calcite ($CaCO_3$) is the main mineral phase of most carbonate sedimentary rocks and their metamorphic

19 equivalents, and is a major component of carbonatites. Calcite is also a common product of hydrothermal alteration and

20 constituent of mineralising systems where it may precipitate from fluids during pre-ore, ore-stage, and post-ore forming

21 processes (Debruyne et al., 2016). The ability to directly date calcite unlocks the possibility to constrain the timing of a vast

22 array of geological processes that can be difficult to date using conventional methods.

23

24 Accurate *in-situ* U–Pb geochronology of calcite has been applied to a variety of geological systems (e.g; Li et al., 2014; Ring

25 and Gerdes, 2016; Roberts and Walker, 2016). However, calcite often incorporates significant quantities of Pb during

26 crystallisation (i.e. 'initial' or 'common' Pb), which can limit the utility of U–Pb geochronology (Rasbury and Cole, 2009).

27 Moreover, Pb is highly fluid mobile (Brugger et al., 2016), so it can be difficult to obtain primary age information with the U–

28 Pb method in hydrothermal or strongly-altered systems (Roberts et al., 2020; Simpson et al., 2021b). Further, given the

29 propensity for calcite to undergo recrystallisation, calcite U–Pb geochronology is rarely applicable to Precambrian systems as

30 the calcite U–Pb system invariably does not remain closed over long timescales.

31

32   Alternative dating systems involving the radiometric decay of rare earth elements (REE) such as Sm–Nd and Lu–Hf, have

33   previously been applied to calcite (e.g. Maas et al., 2020), based on the moderate to strong compatibility of REEs in carbonates

34   in many systems (Debruyne et al., 2016). Importantly for geochronology, experimental evidence indicates that Lu and Hf are

35   highly immobile in many hydrothermal fluids (Brugger et al., 2016; Migdisov et al., 2016), meaning that the Lu–Hf system is

36   less susceptible to resetting during post-formation processes relative to the U–Pb system. However, concentrations of Lu and

37   Hf are generally low (ppm to ppb range) in calcite, necessitating the dissolution of large quantities of material (up to 2g) per

38   sample for conventional Lu–Hf geochronology (Maas et al., 2020). These large quantities significantly reduce the spatial

39   resolution of the technique and have the additional problem of potential contamination from inclusions. Furthermore, age

40   variation is difficult to detect, and bulk samples may produce meaningless mixed ages. The dissolution process also removes

41   calcite from its petrological context. The recent development of *in-situ* Lu–Hf geochronology of individual minerals by LA-

42   ICP-MS/MS allows for rapid acquisition of spatially resolved data (Brown et al., accepted; Glorie et al., 2021; Ribeiro et al.,

43   2021; Simpson et al., 2021a; Tamblyn et al., 2021), opening new avenues for geochronology.

44

45   In this study, we present the first *in-situ* Lu–Hf dating of calcite from a variety of geological environments. We demonstrate

46   the power of *in-situ* calcite Lu–Hf geochronology to produce primary ages for complexly deformed and hydrothermally-altered

47   systems, such as mineral deposits that have previously been difficult, if not impossible, to date using traditional

48   geochronological methods.

49   2 Geological Background of Samples

50   The analysed samples were selected; (1) to demonstrate that calcite Lu–Hf can date primary calcite formation in carbonatites;

51   (2) to reveal the potential of the method to unravel complex ore systems or later events, and; (3) to characterize large calcite

52   samples that would make suitable reference materials for *in-situ* analysis.

53   2.1 Phalaborwa Carbonatite, South Africa

54   The Phalaborwa Igneous Complex is located ~450 km northeast of Johannesburg, in the Limpopo Province, South Africa. The

55   igneous complex is the result of several distinct pulses of alkaline intrusions that were emplaced into Archean granitic gneiss

56   (Staff, 1976). The Loolekop pipe is located in the centre of the Phalaborwa Igneous Complex and was intruded by two episodes

57   of carbonatite emplaced at the intersection of five major faults and shear zones (Basson et al., 2017; Staff, 1976). The oldest

58   carbonatite is termed the "transgressive banded" carbonatite and has an emplacement age of 2060.0 ± 2.2 Ma (Wu et al., 2011).

59   This is intruded by a slightly younger carbonatite termed the "banded" carbonatite and has an emplacement age of $2059.8 \pm$

60   1.3 Ma (Wu et al., 2011). The Phalaborwa carbonatite is unique as it is the only known example of a carbonatite containing

61   economic Cu mineralisation (Groves and Vielreicher, 2001). In the banded carbonatite-phoscorite, Cu mineralisation is

62   primarily in the form of bornite inter-grown with valleriite with minor chalcopyrite (Staff, 1976). In the transgressive

63   carbonatite, Cu mineralisation is present as chalcopyrite inter-grown with cubanite and valleriite (Staff, 1976). Cu

64 mineralisation is interpreted to be magmatic-hydrothermal in origin, with Cu leached by high-temperature hydrothermal fluids

65 at depth, precipitating along fractures within the hosting carbonatite (Le Bras et al., 2021). The sample used in this study (P01)

66 is representative for carbonatite hosted Cu-mineralisation from within the Loolekop pipe (Fig. 1). The sample is

67 mineralogically composed of chalcopyrite inter-grown with cubanite and pyrrhotite alongside an assemblage of magnetite,

68 dolomite, calcite, biotite, pyroxene and valleriite. As the Phalaborwa carbonatite has a well constrained crystallisation age, it

69 provides an ideal case study to demonstrate the utility of the *in-situ* Lu–Hf method for dating igneous calcite directly associated

70 with Cu mineralisation.

71 **2.2 The Eastern Fold Belt, Mt Isa Block, Queensland, Australia**

72 The Eastern Fold Belt of the Mount Isa Domain has experienced multiple episodes of deformation, magmatism,

73 metamorphism, mineralisation and pervasive hydrothermal alteration across the Paleo- to Mesoproterozoic, and hence

74 represents on the most metasomatized crustal blocks on Earth (Oliver et al., 2008). Hydrothermal calcite is common across the

75 region and is spectacularly developed in calcite pods and veins (up to 100s of metres) within the Mary Kathleen Domain

76 (Oliver et al., 1993) and in many of the IOCG deposit of the Cloncurry District. For this study we have selected calcite samples

77 from the Lime Creek calcite quarry and the Mt Elliott IOCG deposit for Lu–Hf analysis. These sample locations have good

78 constraints on expected mineralisation ages, making them suitable samples to demonstrate the technique.

79

80 The Lime Creek quarry is one of number of large calcite pods or veins that are exposed in Mary Kathleen Domain. The Lime

81 Creek quarry is hosted within the ca. 1760 Ma Argylla Formation and lies along the steeply dipping NNW-trending Tribulation-

82 Lime Creek Fault, which offsets regional-scale 'D$_2$' folds (Marshall, 2003). Breccias along this fault contain clasts of calc-

83 silicate rocks and metadiorite clasts with a matrix consisting of albite-actinolite-diopside-biotite-titanite-apatite that are

84 subsequently overprinted by the undeformed Lime Creek calcite-dominated veins (Marshall, 2003). These veins are extremely

85 coarse-grained with calcite crystals larger than 1 m^3, actinolite crystals over 1 m in length, and apatite, biotite, diopside and

86 titanite grains over 20 cm in diameter (Marshall, 2003; Oliver et al., 1993). Based on cross-cutting relationships, it is interpreted

87 that the Lime Creek vein system, and other calcite pods/veins of this style precipitated post-faulting during late-'D$_3$'

88 deformation (ca. 1550–1500 Ma) of the Isan Orogeny (Giles and Nutman, 2002; Marshall, 2003). This style of veining is

89 common throughout the Mary Kathleen Domain and provides evidence of km-scale fluid transport during late-stage

90 metamorphism (Oliver et al., 1993). Based on C and O isotope analysis of calcite from these veins, they are interpreted to have

91 formed from hydrothermal fluids likely associated with the intrusion of the ca. 1530 to 1500 Ma Williams-Naraku Batholiths

92 (Oliver et al., 1993). Although no direct dating has been completed on the Lime Creek Quarry, titanite from the nearby and

93 cognate Knobby Quarry have produced three titanite U–Pb ages of 1521 ± 5 Ma, 1527 ± 7 Ma, and 1555 ± 5 Ma (Oliver et al.,

94 2004). The sample analysed in this study (LC1) consists very coarse-grained calcite with coarse-grained diopside collected

95 from a large calcite pod in the Lime Creek Quarry (Fig. 1).

96

97   Mt Elliott is an IOCG deposit located in the Eastern Fold Belt of the Mount Isa Inlier (Duncan et al., 2011). The deposit is

98   situated within northwest striking splays of the Mount Dore Fault (Duncan et al., 2011; Wang and Williams, 2001), and is

99   hosted within skarn-altered and deformed phyllites and schists (Garrett, 1992; Wang and Williams, 2001). The host rocks were

100   metamorphosed to lower amphibolite facies during the ca. 1600-1580 Ma 'D$_2$' deformation of the Isan Orogeny (Garrett, 1992;

101   Wang and Williams, 2001). The formation of early albite-hematite (red rock) alteration enhanced brittle fracturing and

102   brecciation of the shale (Garrett, 1992). This was infilled by two stages of open-space skarn development: (1) diopside-

103   magnetite-hematite-calcite-titanite-allanite-phlogophite, and: (2) actinolite-scapolite-magnetite-andradite-calcite-epidote-

104   allanite-chllorite and biotite (Garrett, 1992; Wang and Williams, 2001). Sulphides in the second stage include chalcopyrite,

105   pyrrhotite and pyrite (Garrett, 1992). Although the two skarn assemblages are difficult to distinguish mineralogically, the

106   second episode is the most widespread and represents the major Cu–Au event (Garrett, 1992; Wang and Williams, 2001). A

107   variety of geochronological techniques have been applied to constrain the age of Cu–Au mineralisation. The earliest phase of

108   skarn development has been dated at 1530 ± 11 Ma (U–Pb titanite; Duncan et al., 2011). The second stage of skarn development

109   associated with Cu–Au mineralisation has been dated at 1513 ± 5 Ma (molybdenite Re–Os; Duncan et al., 2011) and $1510 \pm$

110   3 Ma (actinolite Ar–Ar; Wang and Williams, 2001). Two outcrop samples from the Mount Elliot Cu–Au deposit were selected

111   for Lu-Hf geochronology. Mt Elliott 1 (ME 1) consists of coarse-grained pink-coloured calcite that is coeval with the formation

112   of diopside, scapolite and magnetite (Fig. 1). Although the paragenesis of this sample is relatively unconstrained, the lack of

113   sulphides may indicate that this sample belongs to the early pre-mineralisation skarn assemblage. Calcite from sample Mt

114   Elliott 2 (ME 2) is coeval with the formation of andradite, pyrite, chalcopyrite, pyrrhotite and magnetite (Fig. 1). The close

115   relationship between calcite and chalcopyrite in this sample indicates that it is associated with the main Cu–Au bearing skarn

116   assemblage.

2.3 Flin Flon Volcanic Massive Sulphide (VMS) Deposit, Canada

118   The Flin Flon Greenstone Belt stretches across central Manitoba through to east central Saskatchewan and hosts several world-

119   class Zn–Cu VMS deposits including the Flin Flon, Callinan and 777 deposits (Koo and Mossman, 1975). Zn–Cu

120   mineralisation is interpreted to have formed contemporaneously with deposition of the 1888.9 ± 1.6 Ma Millrock member

121   during the Trans-Hudson Orogeny (Gibson et al., 2012; Koo and Mossman, 1975; Rayner, 2010). The Flin Flon Zn-Cu orebody

122   is recognised to have undergone six distinct deformation events that have affected the shape of the deposit (Lafrance et al.,

123   2016; Schetselaar et al., 2017). 'D$_1$' and 'D$_2$' were associated with the intra-oceanic accretion of the Flin Flon Arc to other

124   volcanic terrains before ca. 1872 Ma (Lafrance et al., 2016). 'D$_3$' occurred from 1847–1842 Ma as a response to the final

125   accretion of the Flin Flon Terrane to the Glennie Terrane, producing west-verging folds within stacked, east dipping thrust

126   sheets of basement and cover rocks bounded by NNW-striking thrust faults (Lafrance et al., 2016). 'D$_4$' resulted from the

127   collision between the Flin Flon and Glennie complex with the Sask Craton and is broadly coeval with the ca. 1840 Ma Phantom

128   Lakes dyke (Gibson et al., 2012; Lafrance et al., 2016). 'D$_5$' deformation produced a penetrative regional cleavage (S$_5$) that is

129   defined by a continuous chloritic foliation ubiquitous in the volcanic basement rocks (Gibson et al., 2012; Lafrance et al.,

130 2016). EWE–WNW directed compression during 'D$_6$' deformation produced a second regional penetrative cleavage and

131 reactivated a variety of regional-scale faults (Gibson et al., 2012; Lafrance et al., 2016). Regional greenschist to granulite facies

132 metamorphism is associated with D$_{5-6}$ deformation at ca. 1820–1790 Ma (Schneider et al., 2007). The Flin Flon mine horizon

133 was imbricated during 'D$_3$' thrusting with the shape of the ore lenses moulded during 'D$_4$' and 'D$_5$' deformation (Schetselaar

134 et al., 2018). Regional greenschist to amphibolite grade metamorphism occurred between 1820 – 1790 Ma (U-Pb monazite;

135 Schneider et al., 2007), with rocks in the Flin Flon deposit reaching greenschist facies (Koo and Mossman, 1975). The sample

136 selected for this study is from the hydrothermally altered and sheared footwall of the Flin Flon VMS deposit. This sample is

137 composed of highly foliated chlorite and calcite with disseminated pyrite and residual titanomagnetite. A band of highly

138 foliated calcite was selected for Lu–Hf analysis (sample FF014; Fig. 1) to constrain the age of syn-metamorphic shearing of

139 the deposit.

2.3 Yates U-Th prospect, Otter Lake Area, Grenville Province, Canada

141 The Otter Lake area is located in SE Ontario within the Grenville Province. The Grenville Province can be distinguished from

142 surrounding provinces based on various structural, metamorphic and isotopic signatures attributed to the overprinting ca. 1080–

143 985 Ma Grenvillian Orogeny (Rivers, 2015). This orogenic event produced widespread metamorphism from granulite to

144 amphibolite facies between ca. 1090–990 Ma (Breemen and Corriveau, 2005), accompanied by widespread hydrothermal

145 alteration in the Otter Lake area (Kretz et al., 1999). The Yates U-Th prospect is located approximately 100 km northwest of

146 Ottawa, and is renowned for the occurrence of pegmatites that contain large euhedral crystals of apatite set within a matrix of

147 predominantly orange-pink calcite, with diopside, allanite, titanite, fluorite, thorite and phlogopite (Schumann et al., 2019). A

148 wide range of dates have been produced from the Yates mine; including titanite Pb–Pb and U–Pb ages between ca. 1020 and

149 998 Ma (Frei et al., 1997; Kennedy et al., 2011); apatite Pb–Pb, and U–Pb ages of 913 ± 7 Ma (Barfod et al., 2005), 933 ± 12

150 Ma and 920 – 850 Ma (Chew et al., 2011; Xiang et al., 2021) respectively, and an apatite Lu–Hf age of 1031 ± 6 Ma (Barfod

151 et al., 2005). In addition, Simpson et al. (2021a) obtained an *in-situ* Lu-Hf apatite age of 1000 ± 11 Ma (when corrected for

152 laser induced elemental fractionation). Importantly, the apatite Lu–Hf and Pb–Pb ages have been obtained from the same large

153 apatite crystal, indicating that the Lu–Hf and U–Pb systems have been decoupled (as opposed to multiple generations of apatite

154 growth). Barfod et al. (2005) argued that late-stage fluid interactions may have affected Pb retentivity in the apatite, as the

155 apatite was unlikely to be above the apatite Pb closure temperature at ca. 913 Ma. Calcite from a specimen containing coarse-

156 grained euhedral apatite with pink calcite, quartz and diopside was selected for calcite Lu–Hf analysis (OL-MB, Fig. 1). The

157 apatite is enclosed in the sampled calcite, and is interpreted to have crystallised just prior to the calcite, but during the same

158 hydrothermal event.

3 Method

160 The samples were mounted in 2.5 cm diameter epoxy mounts and screened for Lu concentration by LA-ICP-MS to determine

161 suitability for Lu–Hf analysis (Supplementary File 2). Mineral liberation analysis (MLA) maps were obtained using a Hitachi

162 SU3800 scanning electron microscope (SEM) to reveal the petrogenetic context of the analysed calcite.

3.1 In-Situ Lu-Hf Dating Method

164 Analysis was conducted at Adelaide Microscopy, The University of Adelaide. Calcite samples were analysed using a

165 RESOlution 193 nm laser ablation system (Applied Spectra) with a S155 sample chamber (Laurin Technic). The laser ablation

166 system was coupled to an Agilent 8900 tandem mass spectrometer (ICP-MS/MS). The methodology largely follows that of

167 Simpson et al. (2021a) including an initial instrument tune conducted with no NH_3 in the reaction cell to achieve robust plasma

168 conditions (U/Th = 1.00-1.05) and minimal oxide interferences (ThO/Th <0.2%). A carrier gas of 3.5 mL/min N_2 was added

169 after the sample cell in order to increase sensitivity (Hu et al., 2008). Analytical conditions are included in Supplementary

170 Table 1.

171

172 Methods for separation of ^{176}Hf from ^{176}Lu and ^{176}Yb follow that of Simpson et al. (2021a). In more detail, the Agilent 8900x

173 utilises a reaction cell between two quadrupole mass analysers, which can be used to separate isobaric interferences. The first

174 quadrupole is used as a mass filter (e.g., when set to mass 176, only ^{176}Lu, ^{176}Yb, and ^{176}Hf can pass), thereby minimizing

175 potential background interferences and other, unwanted reactions. Following this, a mixture of 10% NH_3 and 90% He is added

176 to the reaction cell (at a rate of 3 mL/min). This mixture is optimized to promote formation of the Hf reaction product

177 $Hf((NH)(NH_2)(NH_3)_3)^+$ and the second quadrupole is set to 82 amu higher than the first (e.g., Q1 = 176 amu and Q2 = 258

178 amu). This method minimizes the equivalent Lu and Yb reaction products, such that the isobaric interferences on ^{176}Hf are

179 negligible (Simpson et al., 2021a). Lens voltages were tuned to increase sensitivity on the Hf reaction product (Simpson et al.,

180 2021a). In order to calculate Lu/Hf ratios, ^{176}Hf (+82) was measured directly, ^{175}Lu was measured as a proxy for ^{176}Lu, and

181 ^{178}Hf (+82) measured as a proxy for ^{177}Hf, with present day isotopic abundances used to convert isotopes (Simpson et al.,

182 2021a). ^{43}Ca was measured for internal normalization of trace element abundances, and the following isotopes were measured

183 to monitor for inclusions: ^{27}Al, ^{47}Ti, ^{89}Y, ^{90}Zr, ^{140}Ce, and ^{172}Yb.

184

185 Lutetium abundances in most calcite samples are low (< 6 ppm), so we employed a large laser diameter of 257 µm, and a

186 repetition rate of 10 Hz to maximize sensitivity. An extra 20 seconds delay was added after each interval of sample ablation

187 in order to ensure the washout had reached background levels. NIST SRM 610 glass was used as the primary reference material

188 and was analyzed using a spot size of 43 µm. The smaller spot size was required to ensure that ^{175}Lu was measured in pulse

189 counting mode (<4 Mcps). Simpson et al. (2021a) demonstrated that there is no downhole fractionation in Lu-Hf isotope ratios,

190 therefore spot sizes do not need to be matched between standards and unknowns.

191

192 A side effect of the use of large ablation spots is 'plasma loading' for which the introduction of a large amount of material

193 reduces the ionizing efficiency of the plasma (Kroslakova and Günther, 2007). Plasma loading was observed in the time

194 resolved signals, with a reduction in signal intensity for all isotopes after ~10 to 15 seconds of ablation. Following this, the

195 signal stabilized after ~18 seconds of ablation (Fig. 2). Importantly, this variation in signal intensity was not observed in the

196 calculated time resolved isotope ratios (Fig. 2), which means that identical ratios were calculated whether this decrease in

197 signal intensity was included or not in the ratio calculation. Importantly, plasma loading can be affected by sample matrix

198 (Kroslakova and Günther, 2007), especially for minerals containing easily ionized elements such as Ca. This necessitates

199 matrix matched calibration, despite the observed lack of down-hole changes in Lu–Hf ratios (Simpson et al., 2021a).

200

201 The large ablation volume caused accumulation of ablated material in the tubing and on the interface cones during the first

202 analytical session, which coincided with a decrease in signal intensity over time. Consequently, session 1 records slightly more

203 signal drift compared to session 2. However, there was no corresponding drift observed in the calculated isotopic ratios, apart

204 from a slight decrease in precision due to the lower sensitivity toward the end of the run. Therefore, we recommend that cones

205 are cleaned prior to analysis, and suggest a maximum session duration of approximately 7 hours when using spot diameters of

206 >200 µm.

207 **3.2 Data Processing**

208 Analysis Trace element concentrations were calculated using standard LA-ICP-MS internal normalization to a major element.

209 For both LA-ICP-MS and LA-ICP-MS/MS analysis, a stoichiometric Ca concentration of 40.04 wt.% for calcite was used.

210 Although the high Ca cps for all analysed samples indicate that they are close to stoichiometric calcite, there may be slight

211 inaccuracies in calculated element concentrations due to major element substitutions from Mg, Fe, and Mn that are common

212 in carbonates. However, element concentrations were largely used as relative proxies to monitor for inclusions.

213 Background subtractions, element concentrations and ratio calculations were performed using LADR software (Norris and

214 Danyushevsky, 2018). Where ^{178}Hf was measured above detection limits, common Hf corrections were applied to the data

215 after background subtractions, but prior to normalization to the standard. In more detail, the ^{178}Hf cps measurement for each

216 sampling cycle of the analysis period of each laser spot was used to calculate the common Hf component of the corresponding

217 ^{176}Hf cps measurement, using the following equation:

218 $$^{176}Hf_r \;=\; {}^{176}Hf_m - \left(\left(\frac{^{176}Hf}{^{178}Hf}\right)c \;\times\; {}^{178}Hf_m\right)$$

219

220

221 Where $^{176}Hf_r$ = radiogenic ^{176}Hf, $^{176}Hf_m$ = measured ^{176}Hf, $^{178}Hf_m$ = the measured ^{177}Hf and $\left(\frac{i^{176Hf}}{i^{178Hf}}\right)c$ = the initial or 'common'

222 $^{176}Hf/^{178}Hf$ ratio. Subsequently, isotopic ratios were corrected using an external reference material bracketing approach

223 (commonly used in LA-ICP-MS geochronology), with primary and secondary reference materials interspaced with unknowns

224 through each analytical session. The data was normalized to NIST SRM 610 glass to correct for drift and matrix independent

225 fractionation using the Lu–Hf isotopic ratios published in Nebel et al. (2009). Following this, $^{176}Hf/^{176}Lu$, $^{176}Lu/^{177}Hf$, and

226 $^{176}Lu/^{176}Hf$ ratios were corrected to MKED calcite, which formed in association with the MKED titanite reference material

227 (1517.32 ± 0.32 Ma, U-Pb TIMS; Spandler et al., 2016). Further details are outlined in supplementary file 3. This correction

228 method is similar to that used by Roberts et al. (2017) for calcite U–Pb, where the observed analytical offset between the

229 measured and expected Lu–Hf ratio in the standard is applied (as a % correction factor) to the ratios of the unknowns. This

230 offset is inferred to be due to a combination of laser induced (matrix-dependent) elemental fractionation and plasma loading.

231 The uncorrected ages for MKED calcite as well as for ME 1 across four analytical sessions are constant within uncertainty,

232 indicating the age offset is a systematic analytical bias that is applicable to the calcite samples of unknown age (Sup. Fig. 3).

233 Weighted average ages were calculated using ISOPLOTR (Vermeesch, 2018), using the ^{176}Lu decay constant determined by

234 Söderlund et al. (2004); 0.00001867 ± 0.00000008 Myr^{-1}

4 Lu-Hf Results

236 The analysed calcite generally contain < 1% common Hf, apart from sample P01, which contains up to 13% common Hf in

237 individual analyses (Table 1). Consequently, the common Hf corrections are small (or effectively non-existent), and the

238 resultant ages are not significantly affected by the assumed initial $^{176}Hf/^{177}Hf$ ratio. Corrected and uncorrected data are included

239 in Supplementary File 1. The weighted mean single-spot Lu–Hf ages, reported below, are corrected against MKED calcite for

240 matrix-dependant fractionation and common-Hf corrected (where relevant) (Fig. 3).

5 Discussion

242 The Phalaborwa carbonatite sample produced an *in-situ* Lu–Hf age of 2054 ± 34 Ma (Fig. 3), consistent with previous

243 baddeleyite U–Pb SIMS ages (~2060 Ma; Wu et al., 2011). Importantly, the consistency between the calcite Lu-Hf age and

244 existing constraints on carbonatite formation demonstrates that calcite Lu-Hf dating can produce primary age information for

245 early Paleoproterozoic calcite. This result also demonstrates that calcite Lu–Hf geochronology is a viable technique to directly

246 date carbonatite magmatism and associated mineralisation, even in the case of old calcite samples with only ~0.5 ppm Lu.

247

248 The calcite Lu–Hf ages for samples ME 1 and ME 2 are 1540 ± 9 Ma and 1500 ± 12 Ma, respectively (Fig. 3). The ages of

249 these samples are consistent with the paragenetic timing of alteration at Mt Elliott, providing evidence for calcite precipitation

250 during at least two temporally distinct alteration events. Sample ME 1 is from a coarse calcite-diopside-scapolite-magnetite

251 vein that does not contain sulfides (Fig. 1), the age is, therefore, consistent with formation prior to the major ~1510 Ma Cu-

252   Au mineralisation event (Duncan et al., 2011; Wang and Williams, 2001). In addition, this age overlaps with a titanite U–Pb

253   age from the Mt Elliott deposit (1530 ± 11 Ma; Duncan et al., 2011), and is potentially related to regional Na-Ca alteration

254   between ca. 1555 and ca. 1521 Ma (Oliver et al., 2004). The 1500 ± 12 Ma age obtained from sample ME 2 that has an ore

255   stage paragenesis conform with the ^{207}Pb/^{206}Pb age of cogenetic andradite (1507 ± 35 Ma; Sup. Fig. 3), and overlaps with the

256   ca. 1510 Ma main mineralisation event (Duncan et al., 2011; Wang and Williams, 2001). These distinct ages obtained for

257   different mineral parageneses from the same IOCG deposit demonstrates the power of in-situ Lu–Hf dating to not only provide

258   direct ages of mineralisation, but also to interrogate multiple alteration events within a single deposit.

259

260   Sample LC1, from the Lime Creek quarry, Eastern Fold Belt, Mt Isa Inlier produced an age of 1513 ± 25 Ma, consistent with

261   published titanite U–Pb ages (1521 ± 5 Ma 1527 ± 7 Ma) from the nearby Knobby Quarry (Oliver et al., 2004). Additionally,

262   this age is consistent with the intrusion of the ca. 1530-1500 Ma Williams-Naraku batholiths, which is interpreted to be the

263   source of the fluids from which the calcite precipitated (Oliver et al., 1993; Page and Sun, 1998). Our results for this sample

264   further demonstrate that calcite Lu–Hf geochronology is an effective technique for constraining the age of calcite

265   mineralisation.

266

267   Sample OL-MB from Otter Lake produced a Lu–Hf age of 892 ± 12 Ma (Fig. 3). This age is significantly younger than the

268   apatite solution Lu–Hf age of 1030 ± 6 Ma (Barfod et al. (2005) and the *in-situ* apatite Lu-Hf age of 1000 ± 11 Ma (Simpson

269   et al. 2021), but is similar to the apatite Pb-Pb age of 913 ± 7 Ma (Barfod et al. 2005) and the latest stage of extensional activity

270   on the nearby Bancroft Shear Zone (1045 - 893 Ma, Ar-Ar phlogopite; Cosca et al., 1995). Given the similarity between the

271   ca. 0.9 Ga ages, obtained by different methods, it seems likely that the calcite either grew or records Lu–Hf isotopic resetting

272   during the same event that induced resetting of the apatite Pb–Pb system. The slight difference between the calcite Lu–Hf age

273   (894 ± 12 Ma) and apatite Pb-Pb age (913 ± 7 Ma) may be due to analytical (i.e. mixing of age domains in the solution Pb-Pb

274   age) rather than geological reasons, particularly given an individual crystal of apatite from the Yates mine produced a U-Pb

275   age range of 920-850 Ma (Xiang et al., 2021). Large (~3cm) apatite crystals such as the one analysed by Barfod et al. (2005)

276   are expected to have Pb closure temperatures of up to 600 °C (Barfod et al., 2005; Krogstad and Walker, 1994), giving a

277   possible upper limit to Lu–Hf closure in calcite. We note that this is significantly higher than the closure temperature of Ar–

278   Ar in phlogopite (ca. 400 °C), indicating that the Otter Lake area potentially had a different thermal history and/or that isotopic

279   resetting in the apatite and calcite was aided by late fluid interactions, as hypothesised by Barfod et al., (2005). As such, further

280   work is required to constrain the Lu–Hf closure temperature in calcite.

281

282   The *in-situ* Lu–Hf age of 1807 ± 19 Ma for the cleavage-hosted calcite vein from the Flin Flon VMS deposit (FF14; Fig. 3),

283   as expected, is younger than the timing of initial mineralisation at the deposit (Koo and Mossman, 1975; Rayner, 2010; Stern

284   et al., 1995). Instead, the age is in excellent agreement with ca. 1820-1790 Ma regional peak greenschist to amphibolite grade

285   metamorphism (Schneider et al., 2007), suggesting the calcite precipitated during metamorphism related to deformation stage

286   'D₅' or 'D₆', associated with the final collision between the Flin Flon-Glennie Complex and the Sask Craton (Lafrance et al.,

287   2016). This regional event locally reached maximum greenschist-facies metamorphism (Koo and Mossman, 1975), suggesting

288   the calcite grew under low-grade metamorphic conditions. Sample FF014, therefore, demonstrates that calcite Lu–Hf

289   geochronology has the potential to date low grade metamorphism, which has been difficult using traditional dating methods

290   (e.g. Henrichs et al., 2018).

291

292   In summary, we demonstrate that *in-situ* Lu–Hf geochronology can produce both accurate and precise (0.5-1.7% uncertainty)

293   ages for calcite from a variety of mineralisation styles (e.g. IOCG, carbonatite, and skarn alteration) as well as greenschist-

294   facies metamorphism. The technique also has great potential to date a range of other geological settings and processes (e.g.,

295   chemical sedimentation, carbonation reactions) provided calcite contains sufficient Lu for analysis.

296   **5.1 Limitations**

297   The success rate of the *in-situ* Lu–Hf dating approach in calcite is intrinsically related to; (1) the concentration of Lu, and; (2)

298   the ingrowth time for radiogenic Hf (Fig. 4). Generally, the method is more suitable for REE-rich calcite typically observed in

299   mineral deposits and carbonatites, and/or for Precambrian samples. In addition, the currently available mass-spectrometers

300   require large laser beam diameters (257 µm) for successful calcite Lu–Hf dating, limiting spatial resolution compared to most

301   laser-ablation dating techniques. However, calcite often forms large, mm to cm scale crystals, reducing the need for small

302   ablation volumes.

303   **5.2 Advantages of in-situ Lu-Hf dating of calcite compared to other geochronological methods**

304   The Previous dissolution-based Lu–Hf geochronology has produced scattered isochrons, indicative of isotopic disturbances

305   (Maas et al., 2020). This is in contrast to the generally well constrained ages demonstrated in this study, highlighting one of

306   the main advantages of the *in-situ* approach: the ability to rapidly obtain high spatial resolution coupled with a much larger

307   number of data points (Simpson et al., 2021a). Importantly, trace element data can be obtained simultaneously to interrogate

308   each data point for inclusions or age zonation. Furthermore, calcite Lu–Hf dating can overcome two issues often encountered

309   during U–Pb dating; (1) in contrast to Pb, calcite does not incorporate significant concentrations of common Hf, and; (2) Lu is

310   comparatively resistant to thermal diffusion in calcite (Cherniak, 1998), increasing the likelihood of primary precipitation ages

311   to be preserved. This opens the possibility that time constraints can be obtained for carbonates from the first three-quarters of

312   Earth history that are generally difficult to date by other methods. Importantly, calcite is commonly associated with ore

313   formation, meaning *in-situ* Lu–Hf dating affords the possibility to directly constrain the age of mineralising events and the

314   temporal evolution of mineral deposit systems.

315

316 From our work, we suggest samples ME1 and OL-MB calcite could be developed as primary reference materials due to being
317 (1) common-Hf free, (2) homogenous in age across crystals up ~1cm cm in size, and (3) available in large quantities. We aim
318 to characterize such reference materials and make them available to the wider geochronology community.

6 Conclusions and Future Directions

320 Calcite is among the most common of rock-forming minerals, meaning that *in-situ* Lu–Hf geochronology of calcite has
321 enormous potential to constrain the age of formation and/or alteration of a range of igneous, sedimentary, metamorphic, and
322 hydrothermal rock systems, including rock-types that are considered very difficult to date (e.g., marbles). This technique has
323 particular application to mineral deposits as it allows for the ability to constrain the age of pre-ore, ore-stage and post-ore
324 events (e.g., Fig. 3). Furthermore, given the successful dating of old (~2 Ga) calcite with <1 ppm Lu (e.g., sample P01; Table
325 1), this technique has the potential to date old calcite from a variety of settings with relatively low HREE concentrations. *In-*
326 *situ* Lu–Hf dating of calcite can be regarded as a complimentary, and in some cases alternative, technique to carbonate U–Pb
327 dating, where Lu–Hf dating is well suited for older samples, or to obtain primary precipitation ages for systems affected by Pb
328 mobility. Coupling *in-situ* Lu–Hf dating with other isotopic systems (U-Th-Pb, C, O, Sr, Nd) may be particularly powerful for
329 constraining the origin, nature and redox conditions of the fluids or melts from which the calcite precipitated.

Author contributions

333 Author contributions: A Simpson (corresponding author): conceptualisation, method development, experimentation,
334 manuscript drafting. S Glorie: conceptualisation, manuscript drafting, primary supervision. M Hand: conceptualisation,
335 manuscript drafting, secondary supervision. C Spandler: Conceptualisation, sampling, manuscript drafting. S Gilbert: Method
336 development, experimentation, manuscript drafting. B Cave. Experimentation, manuscript drafting.

Acknowledgments

339 The authors would like to thank the MinEx CRC for funding this research. The initial method development and apatite dating
340 were supported by the Australian Research Council DP200101881. Dr Anthony Milnes from the Tate Museum at the
341 University of Adelaide is acknowledged for help during sampling and Aoife McFadden is acknowledged for assistance in
342 operating the SEM at Adelaide Microscopy.

References

345 Barfod, G. H., Krogstad, E. J., Frei, R., and Albarède, F., 2005, Lu-Hf and PbSL geochronology of apatites from Proterozoic terranes: A
346   first look at Lu-Hf isotopic closure in metamorphic apatite: Geochimica et Cosmochimica Acta, v. 69, no. 7, p. 1847-1859.
347 Basson, I., Lourens, P., Paetzold, H.-D., Thomas, S., Brazier, R., and Molabe, P., 2017, Structural analysis and 3D modelling of major
348   mineralizing structures at the Phalaborwa copper deposit.: Ore Geology Reviews, v. 83, p. 30-42.

349   Breemen, O. v., and Corriveau, L., 2005, U– Pb age constraints on arenaceous and volcanic rocks of the Wakeham Group, eastern Grenville
350   Province: Canadian Journal of Earth Sciences, v. 42, no. 10, p. 1677-1697.
351   Brown, D. A., Simpson, A., Hand, M., Morrissey, L., Gilbert, S., Tamblyn, R., and Glorie, S., accepted, Laser ablation Lu-Hf dating reveals
352   Laurentian garnet in subducted rocks from southern Australia: Geology.
353   Brugger, J., Liu, W., Etschmann, B., Mei, Y., Sherman, D. M., and Testemale, D., 2016, A review of the coordination chemistry of
354   hydrothermal systems, or do coordination changes make ore deposits?: Chemical Geology, v. 447, p. 219-253.
355   Chew, D. M., Sylvester, P. J., and Tubrett, M. N., 2011, U–Pb and Th–Pb dating of apatite by LA-ICPMS: Chemical Geology, v. 280, no.
356   1-2, p. 200-216.
357   Cosca, M. A., Essene, E. J., Mezger, K., and van der Pluijm, B. A., 1995, Constraints on the duration of tectonic processes: Protracted
358   extension and deep-crustal rotation in the Grenville orogen: Geology, v. 23, no. 4, p. 361-364.
359   Debruyne, D., Hulsbosch, N., and Muchez, P., 2016, Unraveling rare earth element signatures in hydrothermal carbonate minerals using a
360   source–sink system: Ore Geology Reviews, v. 72, p. 232-252.
361   Duncan, R. J., Stein, H. J., Evans, K. A., Hitzman, M. W., Nelson, E. P., and Kirwin, D. J., 2011, A New Geochronological Framework for
362   Mineralization and Alteration in the Selwyn-Mount Dore Corridor, Eastern Fold Belt, Mount Isa Inlier, Australia: Genetic
363   Implications for Iron Oxide Copper-Gold Deposits: Economic Geology, v. 106, no. 2, p. 169-192.
364   Frei, R., Villa, I. M., Nagler, T. F., Kramers, J. D., Pryzbylowicz, W. J., Prozesky, V. M., Hofman, B. A., and Kamber, B. S., 1997, Single
365   mineral dating by the Pb-Pb step leaching method: assessing the mechanisms: Geochimica et Cosmochimica Acta, v. 61, no. 2, p.
366   393-414.
367   Garrett, S. J., 1992, The Geology and Geochemistry of the Mount Elliott Copper-Gold deposit, Northwest Queensland [Masters thesis]:
368   University of Tasmania, 139 p.
369   Gibson, H. L., Lafrance, B., Pehrsson, S., Dewolfe, M. Y., Gilmore, K., and Simard, R.-L., 2012, The Volcanological and Structural
370   Evolution of the Paleoproterozoic Flin Flon Mining District:: Anatomy of a Giant VMS System: Geoscience Canada.
371   Giles, D., and Nutman, A. P., 2002, SHRIMP U–Pb monazite dating of 1600–1580 Ma amphibolite facies metamorphism in the southeastern
372   Mt Isa Block, Australia: Australian Journal of Earth Sciences, v. 49, no. 3, p. 455-465.
373   Glorie, S., Gillespie, J., Simpson, A., Gilbert, S., Khudoley, A., Priyatkina, N., Hand, M., and Kirkland, C. L., 2021, Detrital apatite Lu-Hf
374   and U-Pb geochronology applied to the southwestern Siberian margin: in review.
375   Groves, D. I., and Vielreicher, N. M., 2001, The Phalaborwa (palabora) carbonatite-hosted magnetite-copper sulfide deposit, South Africa:
376   am emd-member of the iron-oxide-copper-gold-rare earth element deposit group?: Mineralium Deposita, v. 36, p. 189-194.
377   Henrichs, I. A., O'Sullivan, G., Chew, D. M., Mark, C., Babechuk, M. G., McKenna, C., and Emo, R., 2018, The trace element and U-Pb
378   systematics of metamorphic apatite: Chemical Geology, v. 483, p. 218-238.
379   Hu, Z., Gao, S., Liu, Y., Hu, S., Chen, H., and Yuan, H., 2008, Signal enhancement in laser ablation ICP-MS by addition of nitrogen in the
380   central channel gas: Journal of Analytical Atomic Spectrometry, v. 23, no. 8.
381   Kennedy, A. K., Kamo, S. L., Nasdala, L., and Timms, N. E., 2011, GRENVILLE SKARN TITANITE: POTENTIAL REFERENCE
382   MATERIAL FOR SIMS U-Th-Pb ANALYSIS: The Canadian Mineralogist, v. 48, no. 6, p. 1423-1443.
383   Koo, J., and Mossman, D. J., 1975, Origin and metamorphism of the Flin Flon stratabound Cu-Zn sulfide deposit, Saskatchewan and
384   Manitoba: Economic Geology, v. 70, p. 48-62.
385   Kretz, R., Campbell, J. L., Hoffman, E. L., Hartree, R., and Teesdale, W. J., 1999, Approaches to equilibrium in the distribution of trace
386   elements among the principal minerals in a high-grade metamorphic terrane: Journal of Metamorphic Geology, v. 8, p. 493-506.
387   Krogstad, R., and Walker, R. J., 1994, High closure temperatures of the U-Pb system in large apatites from the Tin Mountain pegmatite,
388   Black Hills South Dakota, USA: Geochemistry, Geophysics, Geosystems, v. 58, p. 3845-3853.
389   Kroslakova, I., and Günther, D., 2007, Elemental fractionation in laser ablation-inductively coupled plasma-mass spectrometry: evidence
390   for mass load induced matrix effects in the ICP during ablation of a silicate glass: J. Anal. At. Spectrom., v. 22, no. 1, p. 51-62.
391   Lafrance, B., Gibson, H. L., Pehrsson, S., Schetselaar, E., Dewolfe, M. Y., and Lewis, D., 2016, Structural reconstruction of the Flin Flon
392   volcanogenic massive sulfide mining district, Sasketchwant and Manitoba, Canada: Economic Geology, v. 111, p. 849-875.
393   Le Bras, L. Y., Bolhar, R., Bybee, G. M., Nex, P. A., Guy, B. M., Moyana, T., and Lourens, P., 2021, Platinum-group and trace elements in
394   Cu-sulfides from the Loolekop pipe, Phalaborwa: implications for ore-forming processes: Mineralium Deposita, v. 56, p. 161-177.
395   Li, Q., Parrish, R. R., Horstwood, M. S. A., and McArthur, J. M., 2014, U–Pb dating of cements in Mesozoic ammonites: Chemical Geology,
396   v. 376, p. 76-83.
397   Maas, R., Apukhtina, O. B., Kamenetsky, V. S., Ehrig, K., Sprung, P., and Münker, C., 2020, Carbonates at the supergiant Olypmic Dam
398   Cu-U-Au-Ag deposit, South Australia part 2: Sm-Nd, Lu-Hf and Sr-Pb isotope constraints on the chronology of carbonate
399   deposition: Ore Geology Reviews.
400   Marshall, L., 2003, Brecciation within the Mary Kathleen Group of the Eastern Succession, Mt Isa Block, Australia: Implications of district-
401   scale structural and metasomatic processes for Fe-oxide-Cu-Au mineralisation. [PhD thesis]: James Cook University.
402   Migdisov, A., Williams-Jones, A. E., Brugger, J., and Caporuscio, F. A., 2016, Hydrothermal transport, deposition, and fractionation of the
403   REE: Experimental data and thermodynamic calculations: Chemical Geology, v. 439, p. 13-42.

404 Nebel, O., Morel, M., and Vroon, P., 2009, Isotope Dilution Determinations of Lu, Hf, Zr, Ta and W and Hf Isotope Compositions of NIST
405   SRM 610 and 612 Glass Wafers: Geostandards and Geoanalytical Research, v. 33, no. 4, p. 487-499.
406 Norris, A., and Danyushevsky, L., 2018, Towars estimating the complete uncertainty budget of quantified results measured be LA-ICP-MS,
407   Goldschmidt: Boston, USA.
408 Oliver, N., Butera, K., Rubenach, M., Marshall, L., Cleverley, J., Mark, G., Tullemans, F., and Esser, D., 2008, The protracted hydrothermal
409   evolution of the Mount Isa Eastern Succession: A review and tectonic implications: Precambrian Research, v. 163, no. 1-2, p. 108-
410   130.
411 Oliver, N. H., Cartwright, I., Wall, V. J., and Golding, S. D., 1993, The stable isotope signature of kilometre-scale fractureddominated
412   metamorphic fluid pathways, Mary Kathleen, Australia: Journal of Metamorphic Geology, v. 11, no. 5, p. 705-720.
413 Oliver, N. H., Cleverley, J. S., Mark, G., Pollard, P. J., Fu, B., Marshall, L. J., Rubenach, M. J., Williams, P. J., and Baker, T., 2004, Modeling
414   the Role of Sodic Alteration in the Genesis of Iron Oxide-Copper-Gold Deposits, Eastern Mount Isa Block, Australia Economic
415   Geology, v. 99, no. 6, p. 1145-1176.
416 Page, R. W., and Sun, S. S., 1998, Aspects of geochronology and crustal evolution in the Eastern Fold Belt, Mt Isa Inlier: Australian Journal
417   of Earth Sciences, v. 45, no. 3, p. 343-361.
418 Rasbury, E. T., and Cole, J. M., 2009, Directly dating geologic events: U-Pb dating of carbonates: Reviews of Geophysics, v. 47, no. 3.
419 Rayner, N. M., 2010, New U-Pb zircon ages from the Flin Flon Targeted Geoscience Initiative Project 2006-2009: Flin Flon and Hook Lake
420   blocks: Geological Survey of Canada, Current Research, 2010-4, p. 1-12.
421 Ribeiro, B. V., Finch, M. A., Cawood, P. A., Faleiros, F. M., Murphy, T. D., Simpson, A., Glorie, S., Tedeschi, M., Armit, R., and Barrote,
422   V. R., 2021, From microanalysis to supercontinents: insights from the Rio Apa Terrane into the Mesoproterozoic SW Amazonian
423   Craton evolution during Rodinia assembly: Journal of Metamorphic Geology.
424 Ring, U., and Gerdes, A., 2016, Kinematics of the Alpenrhein-Bodensee graben system in the Central Alps: Oligocene/Miocene transtension
425   due to formation of the Western Alps arc: Tectonics, v. 35, no. 6, p. 1367-1391.
426 Rivers, T., 2015, Tectonic Setting and Evolution of the Grenville Orogen: An Assessment of Progress Over the Last 40 Years: Geoscience
427   Canada, v. 42, no. 1, p. 77-124.
428 Roberts, N. M. W., Drost, K., Horstwood, M. S. A., Condon, D. J., Chew, D., Drake, H., Milodowski, A. E., McLean, N. M., Smye, A. J.,
429   Walker, R. J., Haslam, R., Hodson, K., Imber, J., Beaudoin, N., and Lee, J. K., 2020, Laser ablation inductively coupled plasma
430   mass spectrometry (LA-ICP-MS) U-Pb carbonate geochronology: strategies, progress, and limitations: Geochronology, v. 2, no.
431   1, p. 33-61.
432 Roberts, N. M. W., Rasbury, E. T., Parrish, R. R., Smith, C. J., Horstwood, M. S. A., and Condon, D. J., 2017, A calcite reference material
433   for LA-ICP-MS U-Pb geochronology: Geochemistry, Geophysics, Geosystems, v. 18, no. 7, p. 2807-2814.
434 Roberts, N. M. W., and Walker, R. J., 2016, U-Pb geochronology of calcite-mineralized faults: Absolute timing of rift-related fault events
435   on the northeast Atlantic margin: Geology, v. 44, no. 7, p. 531-534.
436 Schetselaar, E., Ames, D., and Grunsky, E., 2017, Integrated 3D Geological Modeling to Gain Insight in the Effects of Hydrothermal
437   Alteration on Post-Ore Deformation Style and Strain Localization in the Flin Flon Volcanogenic Massive Sulfide Ore System:
438   Minerals, v. 8, no. 1.
439 Schneider, D. A., Heizler, M. T., Bickford, M. E., Wortman, G. L., Condie, K. C., and Perilli, S., 2007, Timing constraints of orogeny to
440   cratonization: Thermochronology of the Paleoproterozoic Trans-Hudson orogen, Manitoba and Saskatchewan, Canada:
441   Precambrian Research, v. 153, no. 1-2, p. 65-95.
442 Schumann, D., Martin, R. F., Fuchs, S., and de Fourestier, J., 2019, Silicocarbonatitic melt inclusions in fluorapatite from the Yates prospect,
443   Otter Lake, Québec: Evidence of marble anatexis in the central metasedimentary belt of the Grenville Province: The Canadian
444   Mineralogist, v. 57, no. 5, p. 583-604.
445 Simpson, A., Gilbert, S., Tamblyn, R., Hand, M., Spandler, C., Gillespie, J., Nixon, A., and Glorie, S., 2021a, In-situ Lu Hf geochronology
446   of garnet, apatite and xenotime by LA ICP MS/MS: Chemical Geology, v. 577.
447 Simpson, A., Glorie, S., Morley, C. K., Roberts, N. M. W., Gillespie, J., and Lee, J. K., 2021b, In-situ calcite U-Pb geochronology of
448   hydrothermal veins in Thailand: New constraints on Indosinian and Cenozoic deformation: Journal of Asian Earth Sciences, v.
449   206.
450 Söderlund, U., Patchett, P. J., Vervoort, J. D., and Isachsen, C. E., 2004, The 176Lu decay constant determined by Lu–Hf and U–Pb isotope
451   systematics of Precambrian mafic intrusions: Earth and Planetary Science Letters, v. 219, no. 3-4, p. 311-324.
452 Spandler, C., Hammerli, J., Sha, P., Hilbert-Wolf, H., Hu, Y., Roberts, E., and Schmitz, M., 2016, MKED1: A new titanite standard for in
453   situ analysis of Sm–Nd isotopes and U–Pb geochronology: Chemical Geology, v. 425, p. 110-126.
454 Staff, P. M., 1976, The Geology and the economic deposits of copper, iron, and vermiculite in the Palabora Igneous Complex, A brief
455   review.: Economic Geology, v. 71, p. 177-192.
456 Stern, R. A., Syme, E. C., Bailes, A. H., and Lucas, S. B., 1995, Paleoproterozoic (1.90–1.86 Ga) arc volcanism in the Flin Flon Belt, Trans-
457   Hudson Orogen, Canada: contributions to Mineralogy and Petrology, no. 119, p. 117–141.
458 Tamblyn, R., Hand, M., Simpson, A., Gilbert, S., Wade, B., and Glorie, S., 2021, In-situ laser ablation Lu–Hf geochronology of garnet
459   across the Western Gneiss Region: Campaign-style dating of metamorphism: Journal of the Geological Society, p. jgs2021-2094.

460   Vermeesch, P., 2018, IsoplotR: A free and open toolbox for geochronology: Geoscience Frontiers, v. 9, no. 5, p. 1479-1493.
461   Wang, S., and Williams, P. J., 2001, Geochemistry and origin of Proterozoic skarns at the Mount Elliott Cu-Au(-Co-Ni) deposit, Cloncurry
462   district, NW Queensland, Australia: Mineralium Deposita, v. 36, p. 109-124.
463   Wu, F.-Y., Yang, Y.-H., Li, Q.-L., Mitchell, R. H., Dawson, J. B., Brandl, G., and Yuhara, M., 2011, In situ determination of U–Pb ages and
464   Sr–Nd–Hf isotopic constraints on the petrogenesis of the Phalaborwa carbonatite Complex, South Africa: Lithos, v. 127, no. 1-2,
465   p. 309-322.
466   Xiang, D., Zhang, Z., Zack, T., Chew, D., Yang, Y., Wu, L., and Hogmalm, J., 2021, Apatite U-Pb Dating with Common Pb Correction
467   Using LA-ICP-MS/MS: Geostandards and Geoanalytical Research, v. 45, no. 4, p. 621-642.
468

469   **Figures and Tables**
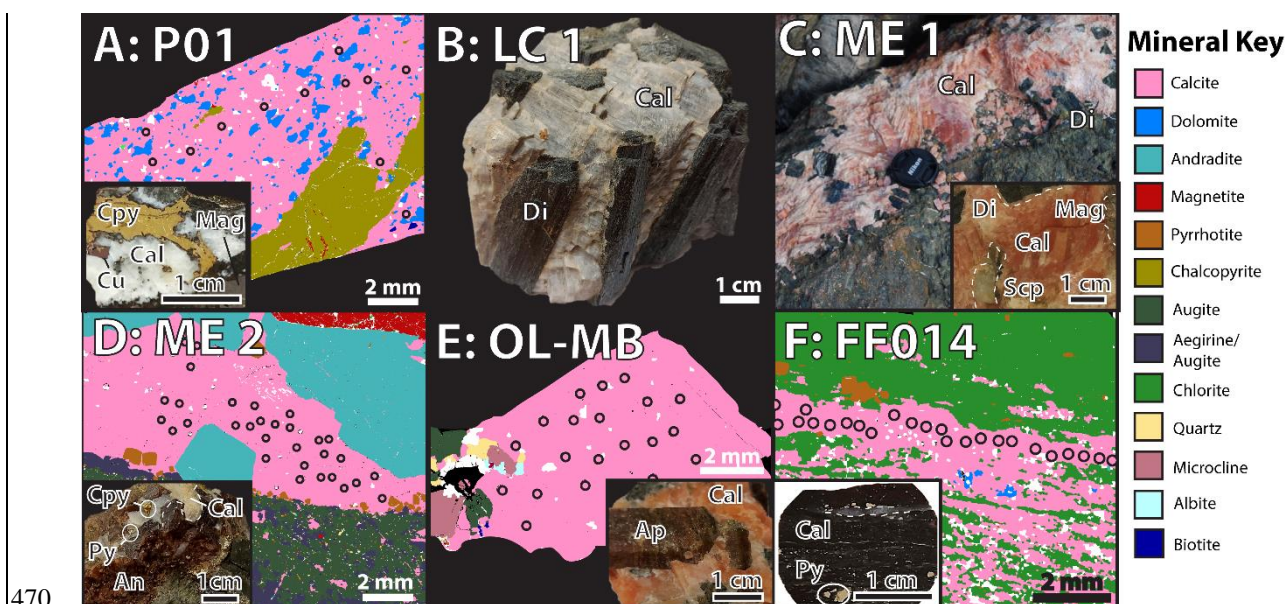
471   **Figure 1: A combination of SEM mineral maps (A,C,D,E) and photos of analysed samples. (A) P01 (Phalaborwa Carbonatite) shows calcite in**
472   **petrogenetic context to chalcopyrite. (B) Photo of LC 1 hand sample. (C) Photo of the ME 1 sample in outcrop, with inset showing the mineralogy of**
473   **the analysed sample. (D) calcite from ME 2 (Mt Isa) in contact with hematite, pyrrhotite and andradite, with inset showing hand sample (D) OL-MB**
474   **(Otter Lake), showing analysed calcite with associated minerals, with inset showing relationship between apatite (Ap) and calcite (Cal) in hand**
475   **sample. (E) FF014 (Flin Flon deposit) shows calcite vein in chlorite matrix with disseminated pyrite, with inset showing analysed block (dark coloured**
476   **matrix is composed of chlorite). Black circles represent laser spot locations. Mineral abbreviations: Cal: Calcite, Cpy: chalcopyrite, Py: pyrite, Mag:**
477   **magnetite, Cu: cubanite, Di: diopside, Scp: scapolite, An: andradite**
478
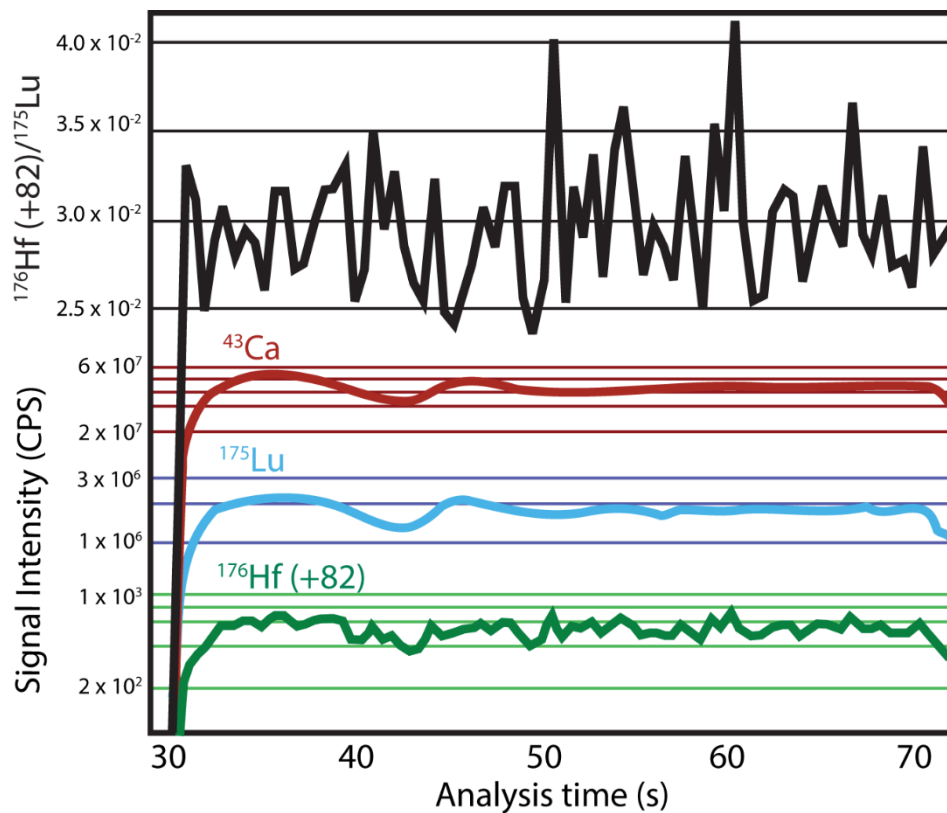
Figure 2: Time resolved signals for ^{175}Lu/$^{(176)}$Hf (+82), ^{43}Ca, ^{175}Lu, and $^{(176)}$Hf (+82) demonstrating the effects of plasma loading on the signal intensities (i.e. dip in signal intensities at ~10-15s ablation), but not for isotope ratios. The time resolved intensity of each analyte has been offset in the graph for better comparison, therefore the Y axis scale is not continuous. Green horizontal lines show the scale for ^{176}Hf (+82), blue horizontal lines show the scale for ^{175}Lu, red horizontal lines show the scale for ^{43}Ca, and black horizontal lines show the scale for the ^{176}Hf (+82)/^{175}Lu ratio. Presented data is from an analysis of MKED calcite.
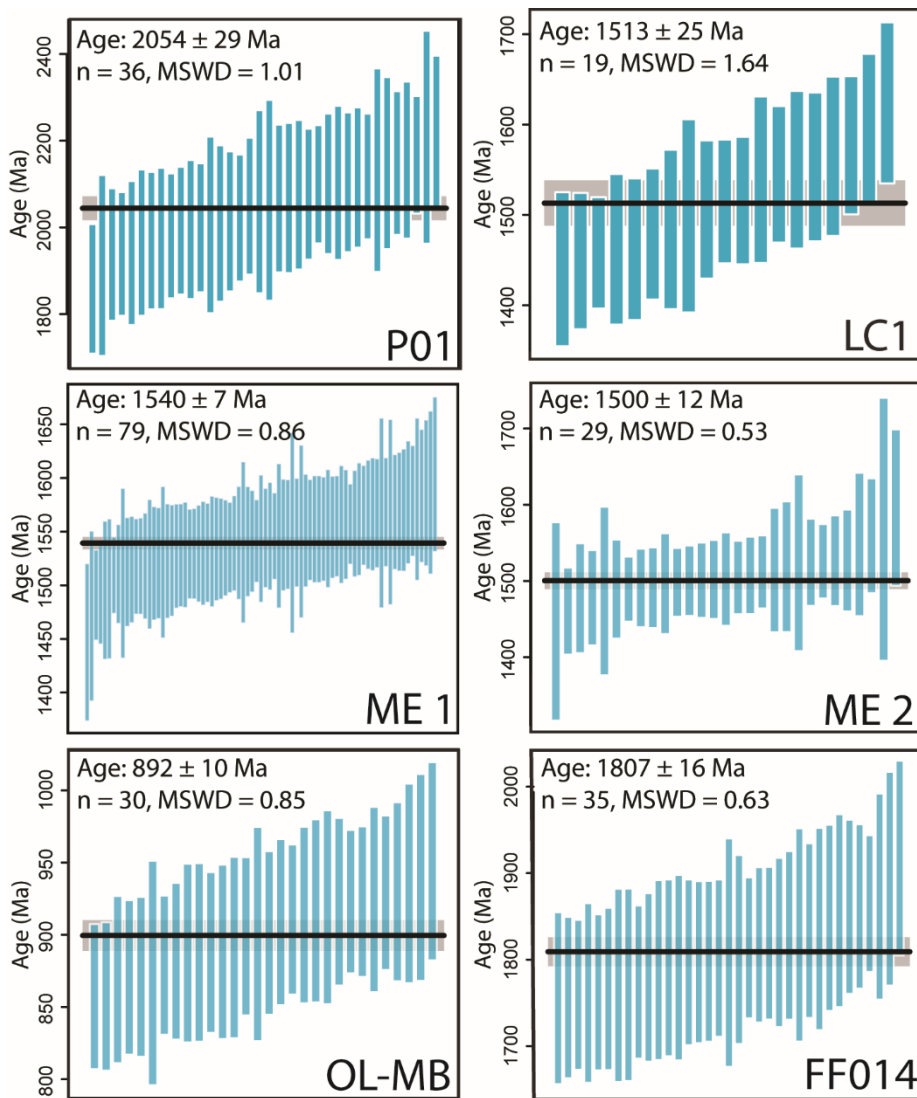
Figure 3: Weighted average 'single spot' ages for analysed samples, corrected for matrix-induced fractionation against MKED1 calcite and for common-Hf where relevant (see Table 1 and text). Blue bars represent 2σ uncertainties. Black lines represent weighted average ages, with grey boxes representing the 95% confidence interval uncertainty.

489
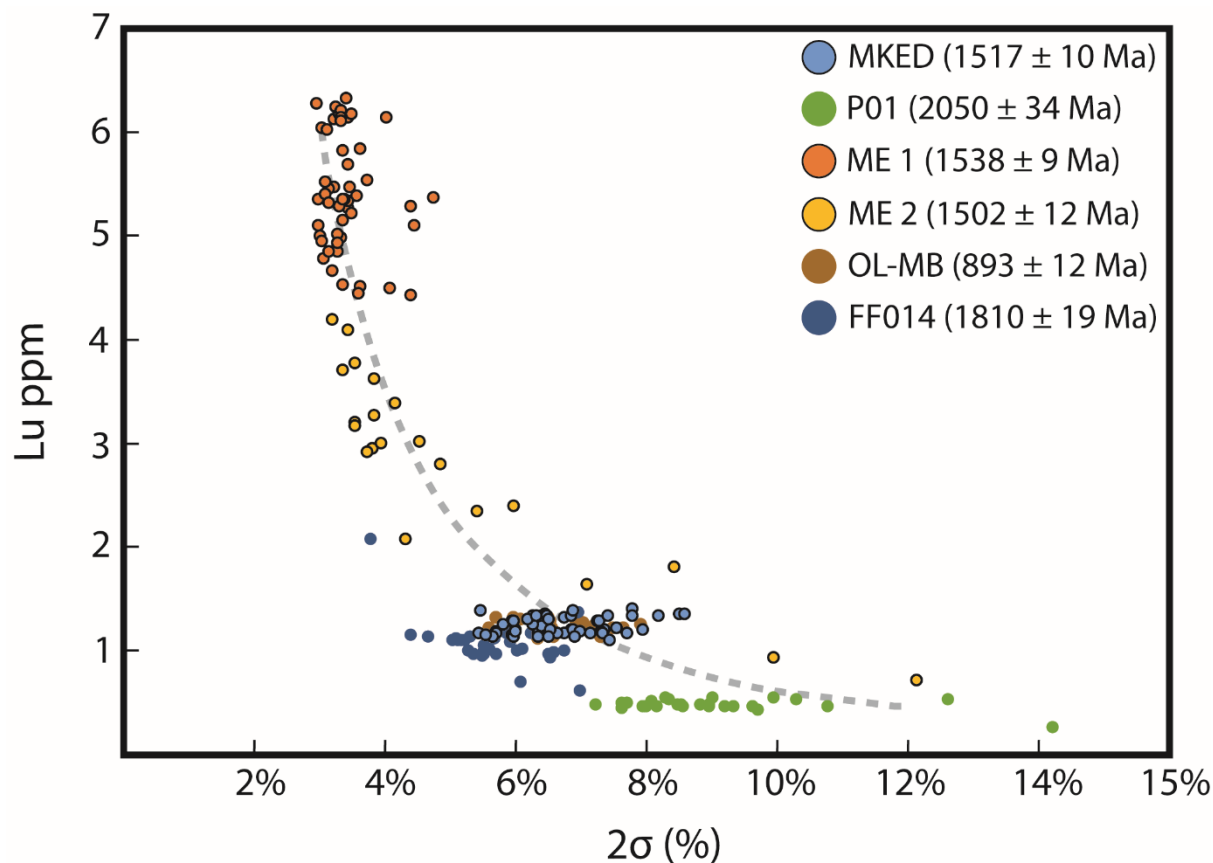
Figure 4: Lu ppm vs 2σ uncertainty for each calcite analysis. The grey curve shows a function fitted to the data from samples with ages between 1500 and 1540 Ma (samples ME1, ME2, and MKED, with symbols outlined in black). Only data points with similar ages were used to construct this guiding curve as the obtained precision is age-dependant. The Lu-Hf ages for older samples (e.g. P01 and FF014) are more precise relative to younger samples for a given Lu concentration (assuming no common Hf). Note: MKED is the calcite Lu-Hf standard used to correct the analysed samples. All data for MKED is included in supplementary file 1.

495

496

497

498

499

500

501

502

503

504

505 TABLE 1: AGES AND LU AND HF CONCENTRATION INFORMATION FOR THE ANALYSED SAMPLES.

Sample	Age (Ma)	95% CI	n	Min. % Hf corr	Av % Hf corr	Max. % Hf corr	Min Lu ppm	Av Lu ppb	Max Lu ppb	Min Hf* ppb	av Hf* ppb	Max Hf ppb
P01	2054	1.4%	36	0%	2.65%	13%	270	505	557	0.03	0.270	1.00
LC 1	1513	1.7%	19	0.16%	0.46%	1.25%	1900	1600	3600	0.011	0.090	0.360
ME 1	1540	0.5%	79	0%	0.28%	2.4%	4300	5325	6300	0.002	0.150	1.80
ME 2	1500	0.8%	29	0.16%	0.58%	3.04%	700	3159	5500	0.002	0.110	0.340
OL-MB	892	1.1%	30	0.16%	0.58%	1.25%	1100	1200	1300	0.003	0.050	0.120
FF014	1807	0.9%	35	0.16%	0.39%	1.3%	616	1020	1170	0.004	0.052	0.210

506 *Note: 95% CI refers to the 95% confidence interval uncertainty on the calculated age. n refers to the number of analyses used for the*

507 *age calculation. % Hf corr refers to the average % decrease in age due to the common Hf correction. Hf* concentrations have been*

508 *calculated from ^{178}Hf and assume no radiogenic ingrowth of ^{176}Hf and thus represent the 'common' Hf concentration for each sample.*

509

510